γ-ray spectroscopy of ^{163}Ta

M. Sandzelius,[1,2,*] B. Cederwall,[1] E. Ganioğlu,[1,5] J. Thomson,[3] K. Andgren,[1] L. Bianco,[3] T. Bäck,[1] S. Eeckhaudt,[2] S. Ertürk,[4] M. B. Gomez Hornillos,[4] T. Grahn,[2,†] P. T. Greenlees,[2] B. Hadinia,[1,‡] A. Johnson,[1] P. M. Jones,[2] D. T. Joss,[3] R. Julin,[2] S. Juutinen,[2] S. Ketelhut,[2] A. Khaplanov,[1] M. Leino,[2] M. Nyman,[2] R. D. Page,[3] P. Rahkila,[2] J. Sarén,[2] C. Scholey,[2] J. Simpson,[4] J. Sorri,[2] J. Uusitalo,[2] and R. Wyss[1]

[1]*Department of Physics, Royal Institute of Technology, S-10691 Stockholm, Sweden*

[2]*Department of Physics, University of Jyväskylä, FIN-40014 Jyväskylä, Finland*

[3]*Oliver Lodge Laboratory, University of Liverpool, Liverpool L69 7ZE, United Kingdom*

[4]*CCLRC Daresbury Laboratory, Daresbury, Warrington WA4 4AD, United Kingdom*

[5]*Science Faculty, Physics Department, Istanbul University, 34459 Istanbul, Turkey*

[6]*Nigde University, Science Faculty, Department of Physics, 51200 Nigde, Turkey*

(Received 12 May 2009; revised manuscript received 22 October 2009; published 25 November 2009)

Excited states in ^{163}Ta have been identified for the first time using the ^{106}Cd(^{60}Ni,3p) fusion evaporation reaction. γ rays were detected using the JUROGAM γ-ray spectrometer and recoil discrimination was achieved using the recoil ion transport unit (RITU) gas-filled separator in conjunction with the GREAT spectrometer situated at the focal plane of the RITU. The yrast states are assigned to a strongly coupled rotational band based on a $\pi h_{11/2}$ configuration. This structure exhibits large signature splitting at low spins that disappears after the paired band crossing because of the alignment of a pair of $i_{13/2}$ neutrons. This effect is ascribed to triaxial shape changes induced by the core-polarizing properties of the deformation-aligned $h_{11/2}$ proton and the rotation-aligned $i_{13/2}$ neutrons. Two additional strongly coupled band structures have been established and are discussed in terms of octupole-vibrational and two-quasiparticle excitations built on the yrast structure. The experimental results are compared with predictions from cranked-shell-model and total-Routhian-surface calculations.

DOI: 10.1103/PhysRevC.80.054316 PACS number(s): 21.10.Re, 23.20.Lv, 25.70.Gh, 27.70.+q

I. INTRODUCTION

The light neutron-deficient odd-A tantalum isotopes are predicted to have near-prolate deformations of $\beta_2 \sim 0.2$–0.3 [1–3] and exhibit rotational bands built on different quasiparticle configurations. This behavior has been observed down to the $N = 92$ nucleus ^{165}Ta [1]. Excited states have also been observed in the lightest known ^{157}Ta [4] and ^{159}Ta [5] nuclei. For these neutron-deficient nuclei, which approach the $N = 82$ shell closure, mean field calculations predict decreasing quadrupole deformation and softening of the nuclear potential with respect to the triaxial deformation parameter γ. Depending on the magnitude and nature of the nuclear deformation, the positions of different single-particle orbitals will change relative to the Fermi surface. Odd-Z, even-N nuclei in this mass region are therefore of key interest because the coupling of the odd proton to the rotating deformed even-even core can serve as a probe of the nuclear structure, providing valuable tests of nuclear models.

One striking phenomenon observed in the neutron-deficient odd-Z, even-N $_{71}$Lu, $_{73}$Ta, $_{75}$Re, and $_{77}$Ir nuclei is the signature splitting observed in the yrast band built on deformed high-K Nilsson states of $\pi h_{11/2}$ origin. This is often illustrated by plotting the energy staggering of the energy levels for the signature partner bands, which is generally found to increase as the neutron number decreases to $N \sim 90$ [1,6–9]. The increased signature splitting is believed to be associated with a substantial negative γ deformation ($\gamma \lesssim -15^\circ$). Given that the nuclear potential is sufficiently soft (i.e., susceptible to the deformation-driving effects of the valence particles), the occupation of orbitals from the upper part of the $\pi h_{11/2}$ shell may drive a prolate-deformed nucleus toward negative γ deformations [10]. The experimentally observed occurrence of signature splitting in this mass region can therefore be qualitatively explained by the triaxial shapes induced by such configurations.

Nuclei exhibiting a potential energy surface that is soft with respect to changes in the nuclear shape are naturally susceptible to shape vibrations. γ- and β-type vibrational excitations are commonly observed in the rare-earth region. Octupole vibrations are, however, much less prolific. Microscopically, correlations between single-particle levels differing by $\Delta l = \Delta j = 3$ can induce octupole-vibrational excitations, but it appears that the conditions necessary for this to occur are rarely met across the nuclear chart. For ^{163}Ta, the Fermi level at a moderate quadrupole deformation lies close to Nilsson states of $d_{5/2}$ and $h_{11/2}$ parentage for protons and close to Nilsson states of $f_{7/2}$ and $i_{13/2}$ parentage for neutrons. Hence, it is a favorable case to search for experimental evidence of octupole-vibrational excitations.

This work reports on the first observation of excited states in ^{163}Ta. Three distinct rotational band structures are found. The underlying configurations are discussed in terms of the deduced rotational and electromagnetic properties and

*Corresponding author: sandzelius@nuclear.kth.se

†Present address: Oliver Lodge Laboratory, Department of Physics, University of Liverpool, Liverpool, L69 7ZE, United Kingdom.

‡Present address: University of the West of Scotland, Nuclear Physics Group, School of Engineering and Science, High Street, Paisley PA1 2BE, Scotland, United Kingdom.

compared with results from cranked-shell-model (CSM) and total-Routhian-surface (TRS) calculations.

II. EXPERIMENTAL DETAILS

The experiment was performed at the Accelerator Laboratory of the University of Jyväskylä employing the K130 cyclotron. Excited states in ^{163}Ta were populated using the ^{106}Cd(^{60}Ni,$3p$) fusion-evaporation reaction at a bombarding energy of 270 MeV. The enriched ^{106}Cd target consisted of a 500 μg/cm^2 self-supporting metallic foil. The average beam intensity was ∼4.4 pnA over 6 d of irradiation time. Prompt γ rays were detected at the target position by the JUROGAM array consisting of 43 EUROGAM phase I and GASP-type [11,12] Compton-suppressed high-purity germanium detectors. The germanium detectors were distributed in six rings at six different angles relative to the beam direction, with five detectors at 158°, ten at 134°, ten at 108°, five at 94°, five at 86°, and eight at 72°. In this configuration, JUROGAM had a total photopeak efficiency of 4.2% at 1.3 MeV.

The fusion-evaporation products were separated in flight from fission products and scattered beam particles using the RITU gas-filled recoil separator [13,14] and subsequently implanted at the focal plane into the double-sided silicon strip detectors (DSSDs) of the GREAT spectrometer. The GREAT [15] spectrometer is a composite detector system that, in addition to the two DSSDs, comprises a multiwire proportional counter (MWPC), an array of 28 Si PIN diode detectors, a segmented planar germanium detector, and a clover germanium detector. Each DSSD has an effective area of 60×40 mm^2, with 200 individual strips at a pitch of 1 mm in both directions, leading to 4800 independent pixels in total. Two additional clover germanium detectors were placed around the focal plane for the detection of delayed γ rays in this experiment. All detector signals were recorded independently using a triggerless total-data-readout (TDR) acquisition system [16], by which they were given a time stamp of 10-ns precision. This allowed for accurate temporal correlations between prompt γ rays detected at the target position and recoil implants at the RITU focal plane and for their subsequent radioactive decays to be performed. Spatial and temporal correlations in the recorded data were analyzed on and off line using the GRAIN software package [17].

The recoil-decay-tagging (RDT) technique [18,19] can be used to identify prompt γ-ray transitions in some nuclides by correlating them with subsequent characteristic α decays detected in the DSSDs of the RITU focal plane. However, a clean, prompt γ-ray spectrum containing only γ-ray transitions belonging to ^{163}Ta could not be obtained in this way. With the relatively high count rate of ∼3 kHz in the DSSD during the experiment, the long correlation time between recoil implantations, and the α decay of ^{163}Ta ($t_{1/2} = 10.9(14)$ s [20] and $b_\alpha \approx 0.2\%$ [21]), the probability was high that a second (or further) recoiling residue would strike the same pixel in the DSSD before the first residue had time to α decay. Therefore, identification and assignments of γ-ray transitions from excited states of ^{163}Ta had to be made from a recoil-correlated spectrum. The recoiling residues were discriminated from scattered beam components by means of the energy loss (ΔE) in the MWPC and the time of flight between the MWPC and the DSSD.

In the off-line analysis, the JUROGAM data were used to construct a three-dimensional symmetric E_{γ_1}-E_{γ_2}-E_{γ_3} cube and asymmetric matrices for determination of γ-ray multipolarities by means of directional correlation of decays from oriented states (DCOs). Coincidence relationships in the matrices and the cube were established using the RADWARE software package [22].

III. EXPERIMENTAL RESULTS

Part of the α-particle energy-decay spectrum of all the radioactive decays in the DSSD following a recoil implantation can be seen in Fig. 1. The spectrum is produced by applying a maximum correlation time of 30 s between a recoil implantation and the subsequent decay. Although ^{163}Ta has a very weak α-decay branch ($b_\alpha \approx 0.2\%$), the $3p$ reaction channel is by far the strongest in the experiment; hence, a peak from its α decays can be clearly seen at an energy of $E_\alpha = 4630$ keV. Using the background-subtracted intensity for the ^{163}Ta α peak, for which the entire α-particle energy was deposited in the DSSD, an average α-decay rate of 143 α particles per minute could be determined. Assuming a 4.4-pnA average beam intensity, a 0.2% α-branching ratio, a 40% transmission through the RITU, and a 55% efficiency for a full α-energy deposition in the DSSD, a cross section for the $^{60}\text{Ni} + {}^{106}\text{Cd} \rightarrow {}^{163}\text{Ta}^* + 3p$ reaction of around $\sigma \approx 70$ mb is estimated.

Figure 2(a) shows a prompt JUROGAM spectrum containing γ rays associated with an implanted fusion-evaporation residue in the DSSD. The γ rays from the main fusion-evaporation channels are marked with various symbols as indicated in the legend. In addition, the three-particle exit channel leading to ^{163}W ($2pn$) and four-particle exit channel leading to ^{162}W ($2p2n$) are shown in Figs. 2(b) and 2(c).

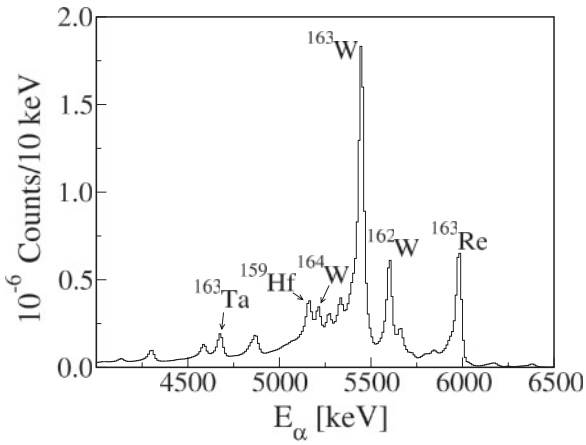

FIG. 1. α-particle energy spectrum from radioactive decays in the DSSD correlated with a preceding recoil implantation in the same pixel. A maximum correlation time (search time) of 30 s is set between a recoil implantation and the subsequent radioactive decay. The α decays from some of the most strongly populated fusion-evaporation channels are indicated above their respective peaks.

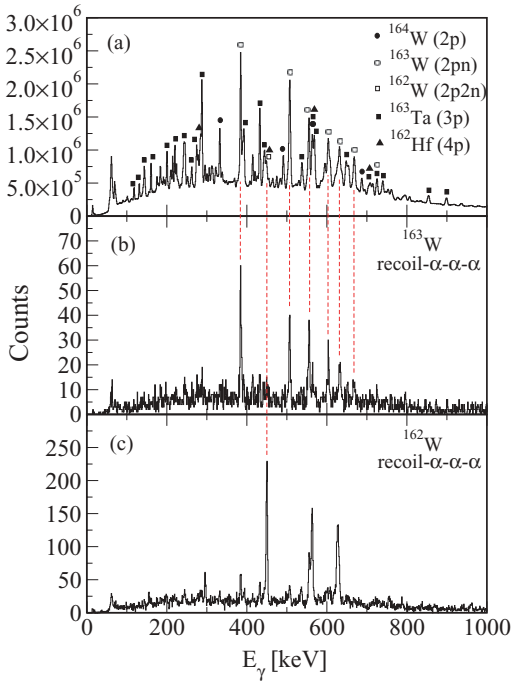

FIG. 2. (Color online) (a) γ-ray energy spectrum in coincidence with any fusion-evaporation residue detected in the DSSD. (b) Recoil-mother-daughter-granddaughter-tagged γ-ray energy spectrum of ^{163}W. (c) As in (b), but correlated with the α-decay chain starting with ^{162}W [23]. When correlating the decays, the search time between subsequent α decays is set to about three half-lives in all cases.

Gamma rays from ^{163}W and ^{162}W are visible in the recoil-correlated spectra [Fig. 2(a)]. The long and cleanly correlated α chains for ^{163}W and ^{162}W enable reliable identification of γ rays from these two competing channels in agreement with the previous observation by Dracoulis *et al.* [23]. Other strong fusion-evaporation channels are the $2p$ and $4p$ channels, leading to ^{164}W [24] and ^{162}Hf [25], respectively. The most intense γ rays, previously assigned to these nuclei, are also indicated in Fig. 2(a).

Because of the unfavorable α-decay characteristics of ^{163}Ta, it was not possible to assign γ rays to ^{163}Ta with the traditional RDT technique by correlating with the subsequent α decays. However, based on the expected population intensity of the $3p$ exit channel, the identification of γ rays from the strongest competing fusion-evaporation exit channels, and Ta x-ray coincidences, the γ-ray transitions indicated in Fig. 2(a) are assigned to originate from decays of excited states in ^{163}Ta. In addition, several of the strongest γ rays here assigned to ^{163}Ta have previously been associated with $A = 163$ [26] using the Daresbury recoil separator. All the γ rays detected in coincidence with these transitions in the recoil-correlated spectrum and with Ta x rays could therefore, without any ambiguity, be assigned to originate from ^{163}Ta.

The γ rays in coincidence with an implanted recoil in the DSSD were sorted into a symmetric E_{γ_1}-E_{γ_2}-E_{γ_3} coincidence cube and analyzed using the LEVIT8R software package [22]. The resulting level scheme for ^{163}Ta is presented in Fig. 3.

Spin assignments are based on the electromagnetic properties of the γ-ray transitions and on the systematics of the heavier odd-A tantalum isotopes ^{165}Ta and ^{167}Ta [1,2], which reveal level schemes similar to that for ^{163}Ta. Further details concerning spin assignments are discussed in Sec. IV. Multipolarities for the strongest transitions in ^{163}Ta have been deduced using a DCO analysis. Using this method the intensity of γ rays measured in the detectors at 94° and at 158° relative to the beam direction were sorted into an asymmetric $\gamma\gamma$-coincidence matrix. The DCO ratios could then be determined through the relation

$$R_{\mathrm{DCO}} = \frac{I_{\gamma_1} \text{ at } \theta_1;\ \text{gated by } \gamma_2 \text{ at } \theta_2}{I_{\gamma_1} \text{ at } \theta_2;\ \text{gated by } \gamma_2 \text{ at } \theta_1}, \qquad (1)$$

where γ_1 and γ_2 are two transitions in mutual coincidence and θ_1 and θ_2 correspond to detectors situated in ring 1 (158°) and ring 5 (94°) relative to the beam direction, respectively. In the JUROGAM geometry, if the gating transition is of a pure stretched quadrupole character, the theoretical values of the R_{DCO} ratios are ∼0.5 for a pure stretched dipole ($M1$ or $E1$) transition and ∼1.0 for a pure stretched quadrupole ($M2$ or $E2$) transition, respectively. The γ-ray energies, relative intensities, DCO ratios, gating transitions, and level spin assignments from the decays of excited states in ^{163}Ta are listed in Table I.

The yrast band structure (labeled as Band 1 in Fig. 3) is a strongly coupled band that extends to spin $I = 57/2$ and excitation energy $E_x = 7212$ keV relative to the bandhead. Figure 4(a) shows a γ-ray spectrum in coincidence with the 288-keV transition. In this spectrum all the γ-ray transitions in Bands 1–3 are visible except the 333- and 433-keV transitions. Figure 4(b) shows only the γ-ray transitions from Band 1. The spectrum is produced by summing the 288, 144, 393, 176, and 475 gates, in each case requiring an additional coincidence with the 201-keV transition. For the lower part of Band 1 the intensity flows mostly via the $E2$ transitions of the favored $\alpha = -1/2$ signature, while for the upper part, above the backbend at spin $I > 31/2^-$, the intensity is carried largely by $M1$ transitions. No transitions depopulating the bandhead have been identified, even though it is not expected to be the ground state. The yrast band structure is associated with the $[514]9/2^-$ Nilsson configuration (as discussed later in this article) and is expected to lie at a rather low excitation energy and to constitute the α-decaying isomeric state with a 10.9-s half-life. Any γ rays depopulating this state could be low in energy and thus below the observable threshold of the focal plane Ge detector. The γ-ray transition depopulating the $11/2^-$ level feeding the $9/2^-$ level would have an energy of only 45 keV. It is not observed in the coincidence spectra in Fig. 4 because it is highly converted and close to the energy threshold of the Ge detectors. Its placement in the level scheme is therefore tentative.

Two additional strongly coupled band structures feeding the yrast band have been observed (labeled as Bands 2 and 3 in Fig. 3). Band 2 depopulates into Band 1 at low spins. The DCO ratios for the 649-, 855-, 900-, and 1070-keV connecting transitions are consistent with $\Delta I = 1$ transitions of dipole character. They are assigned (see Sec. IV) as $E1$ transitions. Band 2 consists of strong $M1$ transitions and generally weak $E2$ transitions and extends to spin $I = 25/2$ and a relative

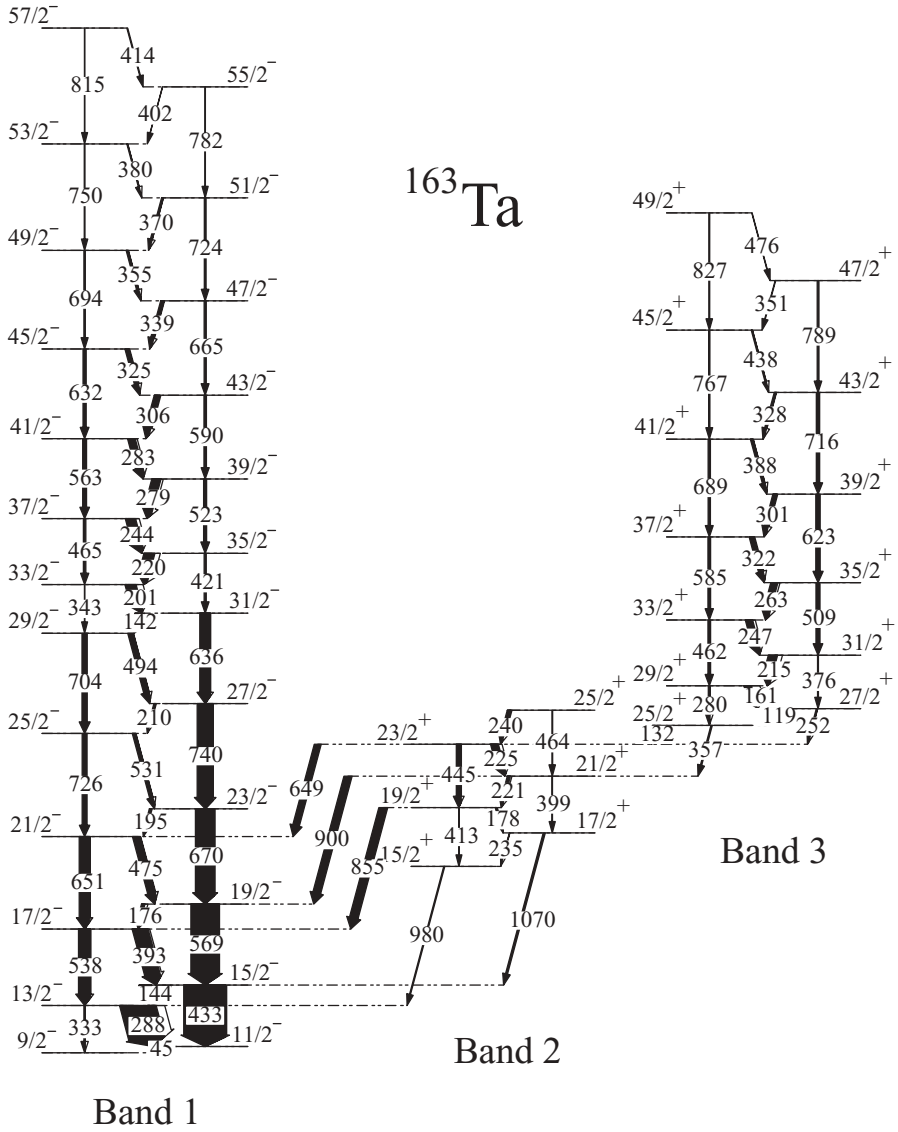

FIG. 3. Level scheme for ^{163}Ta as deduced in the present work. γ rays are labeled with transition energies in keV. The intensity of the transitions is proportional to the width of the arrows. The tentative 45-keV transition in Band 1 was not observed directly but is inferred from the presence of the 333-keV transition.

excitation energy of $E_x = 2411$ keV above the bandhead of Band 1.

Band 3 is also consistent with a strongly coupled structure comprising stronger $M1$ transitions connecting the two signature partner bands and weaker $E2$ transitions, extending to spin $I = 49/2$ and an excitation energy $E_x = 5911$ keV relative to the bandhead of Band 1. γ-ray transitions in Bands 2 and 3 can be viewed in Fig. 4(c). The spectrum is produced by summing all the gates on the $M1$ γ-ray transitions in Band 3 and requiring additional coincidence with the 132-keV transition. Almost all intensity between Bands 3 and 2 flows through the 132-keV transition, which is assigned to be of stretched $M1$ character. The 357- and 252-keV transitions depopulating Band 3 and feeding Band 2 are too weak for any DCO ratios to be deduced. However, because they both most likely change the spin by $2\hbar$ as established from the coincidence relationships, they are interpreted as being predominantly of stretched $E2$ character. This makes the $M1$ dipole assignment of the 132-keV transition and the spin and parity assignments of Band 3 consistent.

IV. DISCUSSION

The rotational band structures observed in ^{163}Ta are consistent with moderately deformed shapes with $\beta_2 \approx 0.2$ (see below). Several Nilsson states are expected to lie close to the Fermi surface in ^{163}Ta at such a deformation. For the heavier tantalum isotopes (e.g., ^{169}Ta), five bandheads are predicted to be below 500 keV [3]. The Nilsson orbitals close to the proton Fermi level are $h_{11/2}\,[514]9/2^-$, $h_{9/2}\,[541]1/2^-$, $g_{7/2}\,[404]7/2^+$, $d_{5/2}\,[402]5/2^+$, and $d_{3/2}\,[411]1/2^+$. The positive-parity states based on the spherical $d_{5/2}$ and $d_{3/2}$ subshells are generally associated with the ground states in the heavier Ta isotopes [2,3]. Configuration assignments of the bands in ^{163}Ta are made later in this article based on the systematics of neighboring isotopes and isotones and on the properties of the bands by examining $B(M1)/B(E2)$ ratios, quasiparticle alignments, and band-crossing frequencies. In Fig. 5, the experimental Routhians and the alignments are plotted for the bands in ^{163}Ta. A rotational reference, with a rotational moment of inertia defined by the Harris parameters [27] $J_0 = 21\hbar^2$ MeV^{-1} and $J_1 = 63\hbar^4$ MeV^{-3}, was subtracted to

TABLE I. γ-ray energies, relative intensities, DCO ratios, gating transitions, and spin-parity assignments for ^{163}Ta. Intensities (I_γ) are adjusted for detector efficiencies and normalized to the strongest transition at $E_\gamma = 288$ keV. Statistical uncertainties are given in parentheses. All spin and parity assignments are tentative.

E_γ (keV)	I_γ (%)	$R_{\rm DCO}$	Gate	$J_i^\pi \rightarrow J_f^\pi$
		Band 1		
(45)[a]				$11/2^- \rightarrow 9/2^-$
141.6(4)	10.0(3)			$31/2^- \rightarrow 29/2^-$
144.2(3)	34.0(7)	0.73(10)	569	$15/2^- \rightarrow 13/2^-$
175.9(4)	9.2(4)	0.71(11)	433	$19/2^- \rightarrow 17/2^-$
195.1(2)	4.4(5)			$23/2^- \rightarrow 21/2^-$
201.0(3)	30.4(10)	0.70(8)	433	$33/2^- \rightarrow 31/2^-$
209.8(2)	4.4(5)			$27/2^- \rightarrow 25/2^-$
220.4(2)	30.0(9)	0.81(10)	433	$35/2^- \rightarrow 33/2^-$
244.3(3)	28.0(7)	0.66(9)	433	$37/2^- \rightarrow 35/2^-$
279.1(2)	20.8(8)			$39/2^- \rightarrow 37/2^-$
283.4(2)	19.8(7)			$41/2^- \rightarrow 39/2^-$
288.1(3)	100.0(13)	0.86(8)	569	$13/2^- \rightarrow 11/2^-$
306.3(3)	15.2(7)			$43/2^- \rightarrow 41/2^-$
325.0(3)	11.2(8)			$45/2^- \rightarrow 43/2^-$
333.1(4)	10.0(6)			$13/2^- \rightarrow 9/2^-$
339.3(4)	4.8(6)			$47/2^- \rightarrow 45/2^-$
342.6(7)	1.0(7)			$33/2^- \rightarrow 29/2^-$
355.2(5)	6.0(7)			$49/2^- \rightarrow 47/2^-$
370.0(2)	4.8(6)			$51/2^- \rightarrow 49/2^-$
379.8(3)	2.4(5)			$53/2^- \rightarrow 51/2^-$
393.4(2)	46.3(9)	0.95(10)	433	$17/2^- \rightarrow 15/2^-$
402.3(4)	<1			$55/2^- \rightarrow 53/2^-$
414.1(5)	1.5(4)			$57/2^- \rightarrow 55/2^-$
421.3(3)	5.6(7)			$35/2^- \rightarrow 31/2^-$
432.9(4)	88.0(13)	1.01(9)	569	$15/2^- \rightarrow 11/2^-$
464.7(2)	6.8(5)			$37/2^- \rightarrow 33/2^-$
475.3(2)	21.2(7)	0.83(12)	569	$21/2^- \rightarrow 19/2^-$
494.3(2)	15.2(4)			$29/2^- \rightarrow 27/2^-$
523.3(4)	8.4(3)			$39/2^- \rightarrow 35/2^-$
531.0(2)	9.6(8)			$25/2^- \rightarrow 23/2^-$
538.2(3)	35.6(9)			$17/2^- \rightarrow 13/2^-$
562.8(3)	10.8(5)			$41/2^- \rightarrow 37/2^-$
569.2(2)	79.6(11)	1.07(8)	433	$19/2^- \rightarrow 15/2^-$
589.6(3)	6.8(4)			$43/2^- \rightarrow 39/2^-$
631.7(4)	8.4(3)			$45/2^- \rightarrow 41/2^-$
636.5(4)	29.5(9)	1.17(12)	433	$31/2^- \rightarrow 27/2^-$
651.2(2)	30.0(9)	1.25(19)	433	$21/2^- \rightarrow 17/2^-$
665.1(3)	6.0(6)			$47/2^- \rightarrow 43/2^-$
670.5(4)	54.0(6)	1.13(12)	433	$23/2^- \rightarrow 19/2^-$
693.6(3)	3.6(4)			$49/2^- \rightarrow 45/2^-$
703.9(4)	14.8(6)			$29/2^- \rightarrow 25/2^-$
723.9(4)	5.2(5)			$51/2^- \rightarrow 47/2^-$
726.3(3)	13.6(5)			$25/2^- \rightarrow 21/2^-$
740.1(3)	44.4(10)	1.08(14)	433	$27/2^- \rightarrow 23/2^-$
750.3(4)	2.0(3)			$53/2^- \rightarrow 49/2^-$
781.8(5)	1.2(3)			$55/2^- \rightarrow 51/2^-$
815.3(4)	<1			$57/2^- \rightarrow 53/2^-$
		Band 2		
178.5(4)	3.2(5)			$19/2^+ \rightarrow 17/2^+$
221.1(3)	8.4(3)			$21/2^+ \rightarrow 19/2^+$
224.6(4)	21.6(7)	0.93(14)	433	$23/2^+ \rightarrow 21/2^+$
235.1(5)	1.2(5)			$17/2^+ \rightarrow 15/2^+$
240.1(3)	9.2(7)			$25/2^+ \rightarrow 23/2^+$
399.2(4)	2.4(7)			$21/2^+ \rightarrow 17/2^+$
413.3(3)	2.4(5)			$19/2^+ \rightarrow 15/2^+$
445.2(3)	14.0(6)	1.0(12)	433	$23/2^+ \rightarrow 19/2^+$
464.1(2)	2.0(5)			$25/2^+ \rightarrow 21/2^+$
648.6(3)	18.8(6)	0.61(20)	569	$23/2^+ \rightarrow 21/2^-$
854.8(4)	24.4(7)	0.73(18)	433	$19/2^+ \rightarrow 17/2^-$
899.6(3)	22.4(7)	0.69(14)	433	$21/2^+ \rightarrow 19/2^-$
979.9(4)	2.8(3)			$15/2^+ \rightarrow 13/2^-$
1069.7(3)	6.0(5)	0.63(22)	433	$17/2^+ \rightarrow 15/2^-$
		Band 3		
118.6(3)	26.4(7)	0.76(21)	433	$27/2^+ \rightarrow 25/2^+$
131.9(3)	31.6(8)	0.76(19)	433	$25/2^+ \rightarrow 23/2^+$(Band 2)
161.1(4)	24.4(8)	0.98(17)	433	$29/2^+ \rightarrow 27/2^+$
215.2(4)	23.2(7)	0.75(18)	433	$31/2^+ \rightarrow 29/2^+$
246.6(3)	20.8(6)			$33/2^+ \rightarrow 31/2^+$
252.1(3)	2.4(3)			$27/2^+ \rightarrow 23/2^+$(Band 2)
262.9(4)	19.2(4)			$35/2^+ \rightarrow 33/2^+$
280.3(5)	4.0(5)			$29/2^+ \rightarrow 25/2^+$
301.1(4)	10.8(6)			$39/2^+ \rightarrow 37/2^+$
322.3(3)	13.2(5)			$37/2^+ \rightarrow 35/2^+$
328.4(3)	5.2(4)			$43/2^+ \rightarrow 41/2^+$
350.7(5)	1.2(4)			$47/2^+ \rightarrow 45/2^+$
357.3(6)	2.8(4)			$25/2^+ \rightarrow 21/2^+$(Band 2)
376.3(4)	2.4(3)			$31/2^+ \rightarrow 27/2^+$
387.7(4)	7.2(6)			$41/2^+ \rightarrow 39/2^+$
438.2(3)	3.2(5)			$45/2^+ \rightarrow 43/2^+$
461.6(4)	7.3(6)			$33/2^+ \rightarrow 29/2^+$
476.4(3)	1.2(4)			$49/2^+ \rightarrow 47/2^+$
509.4(3)	10.8(7)			$35/2^+ \rightarrow 31/2^+$
585.1(4)	7.2(5)			$37/2^+ \rightarrow 33/2^+$
623.3(3)	11.4(6)			$39/2^+ \rightarrow 35/2^+$
688.5(4)	6.4(5)			$41/2^+ \rightarrow 37/2^+$
715.7(4)	9.6(6)			$43/2^+ \rightarrow 39/2^+$
766.5(4)	3.2(4)			$45/2^+ \rightarrow 41/2^+$
789.1(3)	4.8(5)			$47/2^+ \rightarrow 43/2^+$
826.6(5)	2.4(4)			$49/2^+ \rightarrow 45/2^+$

[a]The transition is not observed directly but inferred from systematics and the presence of the 333-keV transition.

give a near-constant alignment for the low-spin states. The quasiparticle labeling scheme for the Nilsson orbitals closest to the Fermi surface used in this article is given in Table II.

A. Band 1

The low-spin part (below spin $I \leqslant 31/2$) of the yrast sequence (Band 1; see Fig. 3) is interpreted as a one-quasiparticle (1qp) configuration (e and f configuration), where the odd proton is residing in the $[514]9/2^-$ Nilsson orbital, in agreement with the assignment established for the yrast structures in the heavier $^{165-169}$Ta isotopes. At low spins the band has an alignment of $i_x \approx 1.6\hbar$, which is consistent with the $[514]9/2^-$ Nilsson (e) configuration. At a rotational frequency $\hbar\omega \approx 0.28$ MeV the band exhibits a characteristic backbend, as seen in the alignment plot [Fig. 5(b)].

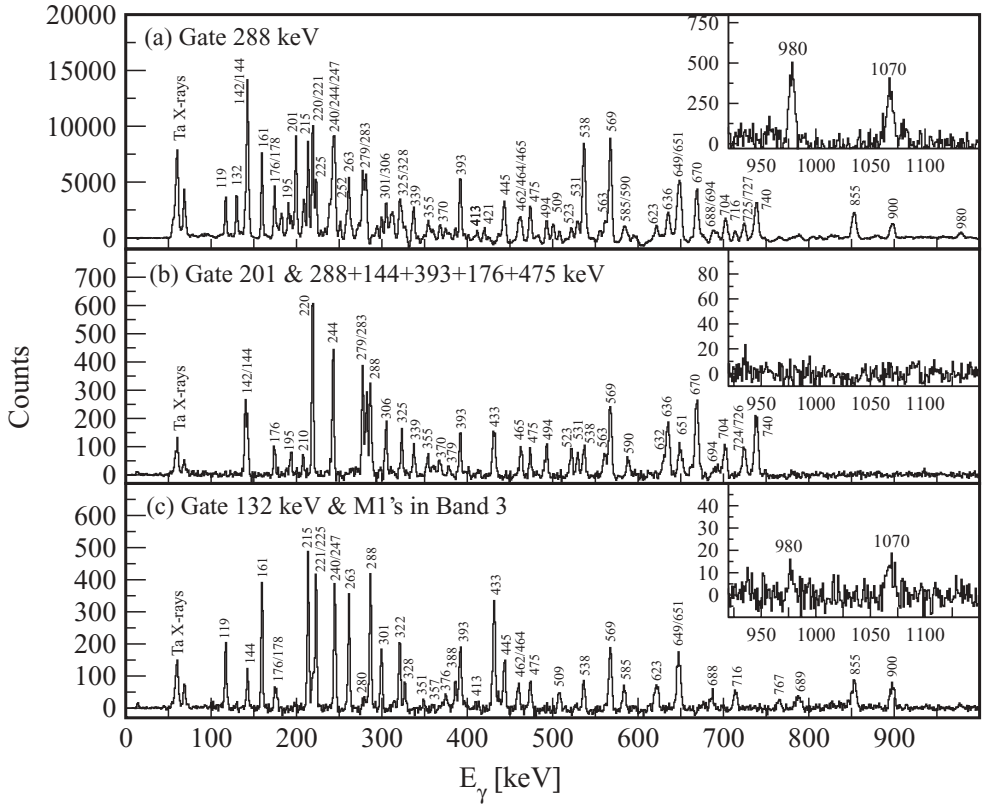

FIG. 4. Coincidence γ-ray spectra generated from a recoil-gated E_{γ_1}-E_{γ_2}-E_{γ_3} coincidence cube with transition energies given in keV. (a) Spectrum showing γ rays in coincidence with the 288-keV transition. (b) Spectrum showing γ rays in coincidence with the 201-keV transition and a sum of gates from the 288-, 144-, 393-, 176-, and 475-keV transitions of Band 1. The spectrum shows members of Band 1 only. (c) Spectrum gated by the 132-keV transition and the sum of gates from all the $M1$ transitions in Band 3, displaying γ rays found in Bands 2 and 3 and the lowest members of Band 1.

The structure above the backbend is interpreted as a three-quasiparticle (3qp) configuration following the breaking of a $\nu i_{13/2}$ neutron pair, with the resulting alignment gain of $\Delta i_x \approx 10.2\hbar$. The crossing frequency predicted by CSM calculations is $\hbar\omega \approx 0.26$ MeV, which is in excellent agreement with the observed one. Such AB crossings are observed systematically at similar rotational frequencies in even-N nuclei throughout this mass region. For instance, the observed crossing frequency and the gain in alignment are identical to those in the even-even neighboring isotone ^{162}Hf ($\hbar\omega = 0.28$ MeV, $\Delta i_x = 10.2\hbar$) [25]. For the heavier odd-A isotopes $^{165-169}$Ta the experimentally observed AB-crossing frequencies are generally slightly lower, $\hbar\omega = 0.24$–0.26 MeV, than in ^{163}Ta. The same trend can be observed in the odd-A isotopes ^{169}Re and ^{167}Re [7,28] and in ^{171}Ir and ^{169}Ir [6,29], where the alignment is delayed by $\sim$50 keV to higher frequencies when the neutron number changes from $N = 94$ to $N = 92$. CSM calculations predict this shift to be $\sim$50 keV between the tantalum isotopes with $N = 92$ (^{165}Ta) [1] and $N = 90$ (^{163}Ta), an expected consequence of the lowering of the neutron Fermi level below the $i_{13/2}$ shell. The same CSM calculations also predict a slight reduction in the interaction strength between the 1qp band and the S band (3qp band following the AB crossing) for ^{163}Ta as compared to the heavier Ta isotopes, and this is indeed also observed.

TABLE II. Labeling convention of the lowest Nilsson orbitals considered for ^{163}Ta described by their parity and signature quantum numbers. Uppercase (lowercase) letters denote neutron (proton) configurations.

Shell-model label	Nilsson label	(π, α)	Label
$\nu i_{13/2}$	$1/2^+[660]$	$(+, +1/2)$	A
$\nu i_{13/2}$	$1/2^+[660]$	$(+, -1/2)$	B
$\nu i_{13/2}$	$3/2^+[651]$	$(+, +1/2)$	C
$\nu i_{13/2}$	$3/2^+[651]$	$(+, -1/2)$	D
$\nu h_{9/2}/f_{7/2}$	$5/2^-[523]$	$(-, +1/2)$	E
$\nu h_{9/2}/f_{7/2}$	$5/2^-[523]$	$(-, -1/2)$	F
$\pi d_{3/2}$	$1/2^+[411]$	$(+, +1/2)$	a
$\pi d_{3/2}$	$1/2^+[411]$	$(+, -1/2)$	b
$\pi g_{7/2}$	$7/2^+[404]$	$(+, +1/2)$	c
$\pi g_{7/2}$	$7/2^+[404]$	$(+, -1/2)$	d
$\pi h_{11/2}$	$9/2^-[514]$	$(-, -1/2)$	e
$\pi h_{11/2}$	$9/2^-[514]$	$(-, +1/2)$	f

To confirm the configuration assignment for the strongly coupled yrast band, $B(M1;\ I \to I-1)/B(E2;\ I \to I-2)$ ratios have been extracted from the experimental branching ratios of competing $\Delta I = 1$ and $\Delta I = 2$ γ-ray transitions. The $B(M1)/B(E2)$ ratios are sensitive to the single-particle configuration, as well as to the nuclear quadrupole deformation. The experimental ratios were compared to theoretical estimates

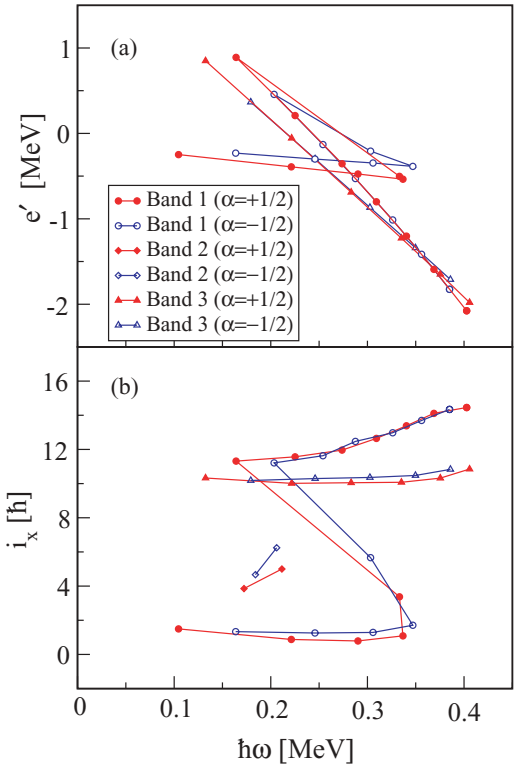

FIG. 5. (Color online) (a) Experimental Routhians for the bands seen in ^{163}Ta. (b) Experimental aligned angular momenta, i_x, relative to a core reference $i_{\rm ref} = J_0\omega + J_1\omega^3$ with $J_0 = 21\hbar^2$ MeV^{-1} and $J_1 = 63\hbar^4$ MeV^{-3} for positive and negative parity bands in ^{163}Ta. In (a) and (b), the positive (negative) signatures are indicated with solid (open) symbols.

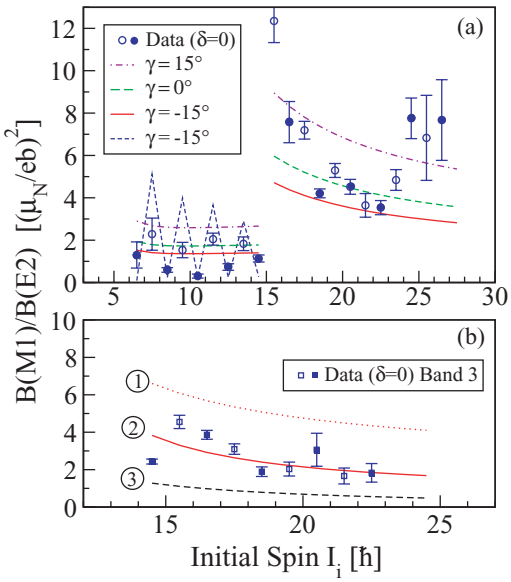

FIG. 6. (Color online) Experimental $B(M1;\ I \to I-1)/B(E2;\ I \to I-2)$ values as a function of initial spin I_i for the strongly coupled bands in ^{163}Ta. The measured values are compared to the predictions of the semiclassical model of Dönau and Frauendorf [30] and Dönau *et al.* [31]. (a) Values for the [514]9/2$^-$ band (Band 1), before and after the AB crossing [e(f) and eAB(fAB) configuration, respectively], are shown here for different γ deformations, as described in the text. A slight staggering of the experimental values is observed between the favored ($\alpha = -1/2$) and unfavored ($\alpha = +1/2$) signature of the strongly coupled yrast band, represented by open and solid symbols, respectively. The staggered dashed line represents the theoretical calculation taking the signature dependent term into account. (b) The curves represent theoretical calculations for Band 3 with the following configurations: 1, $\pi h_{11/2} \otimes AB$; 2, $\pi h_{11/2} \otimes AE$; 3, $\pi g_{7/2} \otimes AB$.

using the semiclassical formalism of Dönau and Frauendorf [30] and Dönau *et al.* [31]. The theoretical calculations use the deformation parameters β_2 and γ obtained from our TRS calculations: $\beta_2 = 0.177$ and $\gamma = -15^\circ$ for the low-spin part of the band and a slightly smaller quadrupole deformation of $\beta_2 = 0.170$ and $\gamma = 0^\circ$ for the high-spin states above the backbend. The single-particle g factors were obtained through the prescription of Schmidt [32] and calculated to be $g_p = 1.21$ for the $h_{11/2}$ proton orbital. Where possible, experimental g factors have been employed for the various quasiparticles involved in the calculations. The rotational g factor g_R was taken to be $Z/A = 0.448$ and the alignments were extracted from the experimental data as described in the caption of Fig. 5. The $E2/M1$ multipole mixing ratios δ were set to zero.

Several possible configurations and deformation parameters are given in Fig. 6 to compare the theoretical estimates with the experimentally extracted branching ratios. For Band 1 below the AB crossing, the data points are in best agreement with this calculation if we assume a negative γ deformation ($\gamma = -15^\circ$) rather than an axially symmetric shape ($\gamma = 0^\circ$). This could be a result of the $h_{11/2}$ valence proton driving the nucleus toward negative γ deformation, giving rise to the large energy splitting of $\simeq$140 keV at low spins between the signature partners in the yrast band of ^{163}Ta by means of enhanced K-mixing, as discussed later in this article. CSM calculations including the γ degree of freedom show a signature favoring negative γ values for the high-K $\pi h_{11/2}$ configuration [2]. When the signature-dependent term ($\pm\Delta e'/\hbar\omega$) is incorporated in the calculation, the splitting between the favored and unfavored signatures is represented by the staggered dashed curve in Fig. 6(a). Although the theoretical values overestimate the $B(M1)/B(E2)$ ratios somewhat, there is overall good agreement with the experimental data. Above the backbend ($I > 31/2$), the experimental $B(M1)/B(E2)$ ratios show a marked increase. This is consistent with an increase in the $B(M1)$ strength attributable to the alignment of the $i_{13/2}$ neutrons but might also reflect a possible change in deformation. The significantly reduced signature splitting observed above the crossing at $\hbar\omega \approx 0.28$ MeV is evidence of the $\nu i_{13/2}$ neutrons polarizing the nucleus away from negative γ values, toward a near-axially symmetric prolate shape. This interpretation is supported by Fig. 6, in which a fit to the experimental $B(M1)/B(E2)$ ratios is best reproduced with $\gamma = 0^\circ$ (or a slightly positive γ value) for the adopted eAB(fAB) configuration.

TRS calculations [33,34] have been performed to interpret the observed band structures. The TRS calculations are

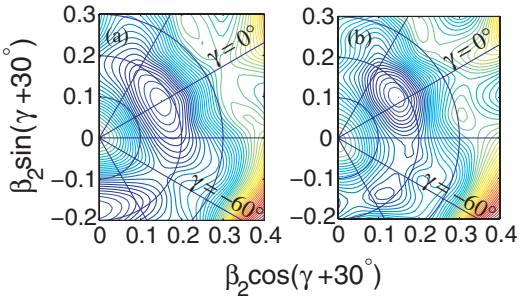

FIG. 7. (Color online) Total Routhian surfaces calculated for the $(\pi, \alpha) = (-, -1/2)$ e configuration of ^{163}Ta showing the deformation parameters β_2 and γ at rotational frequencies $\hbar\omega = 0.0$ MeV (a) and $\hbar\omega = 0.360$ MeV (b). A moderately deformed ($\beta_2 \approx 0.18$, $\gamma \approx 0°$) minimum is observed at both frequencies. The depth of the potential energy surfaces is given by the color coding, where blue (dark gray) shows the lowest energy and red (light gray) the highest. The energy difference between contour lines is 100 keV.

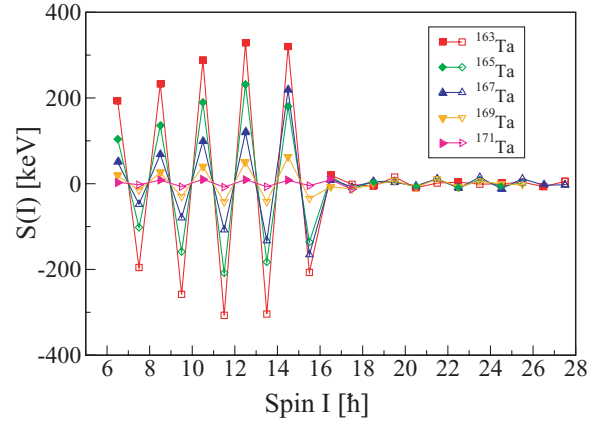

FIG. 8. (Color online) Staggering parameter $S(I)$ as a function of spin I for the $[514]9/2^-$ bands in the neutron-deficient odd-A tantalum isotopes ^{163}Ta, ^{165}Ta [1], ^{167}Ta [2], ^{169}Ta [3], and ^{171}Ta [36]. The solid (open) symbols represent the $\alpha = +1/2$ ($\alpha = -1/2$) signature.

sensitive to a specific nucleonic configuration and show, for each rotational frequency, the total energy in the rotating frame (Routhian) as a function of deformation parameters β_2 and γ. A minimum of such a surface will show the favored deformation for a specific configuration of the nucleus at a specific rotational frequency. The TRS calculations predict an axially symmetric shape, with $\beta_2 \approx 0.18$ and $\gamma \approx 0°$, at low rotational frequencies (see Fig. 7).

CSM calculations show that the occupation of low-Ω orbital from the $i_{13/2}$ neutron spherical subshell drives the nucleus toward positive γ deformation [2]. The alignment of a pair of $i_{13/2}$ neutrons at $\hbar\omega \approx 0.28$ MeV induces a shift in triaxial deformation toward positive γ. Hence, the TRS calculations are not able to reproduce the negative γ deformation deduced from the experimental signature splitting and the $B(M1)/B(E2)$ values below the backbend. However, the predicted core-polarizing effect of the $i_{13/2}$ neutron alignment toward positive γ values is consistent with the observed disappearance of signature splitting [and the $B(M1)/B(E2)$ ratios] after the backbend. If after the band crossing a γ deformation of $\sim 0°$ is assumed, the large signature splitting observed at lower angular momentum should disappear, as is indeed the case.

The signature splitting for Band 1 is illustrated in Fig. 8 using the staggering parameter $S(I)$ [7,35] defined as

$$S(I) = E(I) - E(I-1) - \tfrac{1}{2}[E(I+1) - E(I) + E(I-1) - E(I-2)] \quad (2)$$

and compared with the signature splitting of the corresponding bands in the heavier odd-A tantalum isotopes $^{165-171}$Ta [1–3,36]. The signature splitting can be interpreted as arising from mixing of an $\Omega = 1/2$ component into the high-K $h_{11/2}$ proton configuration. However, because the proton Fermi level is situated high in the $h_{11/2}$ shell, the normal Coriolis mixing of the $\Omega = 1/2$ component into the wave function is expected to be low for an axially symmetric nucleus. Therefore, to reproduce the large signature splitting observed in the high-K $[514]9/2^-$ configuration, a mechanism is needed for enhanced mixing with the $\Omega = 1/2$ orbital. This can be achieved by a departure from an axially symmetric shape [10] for which K is no longer a good quantum number. Figure 8 shows that the signature splitting, as reflected by the staggering parameter, increases toward greater neutron deficiency.

The energy splitting also increases slightly as a function of increasing angular momentum from the bandhead until the band crossing is reached. At low spins, the tantalum isotopes follow the same trend of increasing signature splitting as the odd-mass $^{167-173}$Re [7] and $^{169-173}$Ir [6] isotopes with decreasing neutron number, probably reflecting a general trend of increasing shape asymmetry as the Fermi level decreases in the neutron shell. This trend might be explained by the shape-polarizing properties of the $\pi h_{11/2}$ orbital, which could drive the nucleus toward increasingly negative γ deformations ($\gamma \lesssim -15°$), if the nuclear potential surface becomes softer with respect to the γ degree of freedom. Interestingly, these observations seem not to be supported by the TRS calculations, which predict less pronounced γ deformations for the corresponding quasiparticle configuration with decreasing neutron number. However, it should be noted that an increased γ softness is predicted with increasing neutron deficiency. The "effective" γ deformation of the nuclear wave function may therefore be nonzero. Above the $\nu(i_{13/2})^2$ neutron alignment, the staggering parameter becomes significantly smaller in all odd-mass tantalum isotopes (see Fig. 8), reflecting a reduction in the signature splitting. This is consistent with a transition to an axially symmetric shape.

B. Band 2

Band 2 exhibits an alignment of $\sim 5\hbar$ at $\hbar\omega \approx 0.20$ MeV and has a larger moment of inertia than the yrast band in the same rotational frequency range (see Figs. 5 and 9). This relatively large alignment and the moment of inertia are difficult to reconcile with a pure 1qp configuration based on

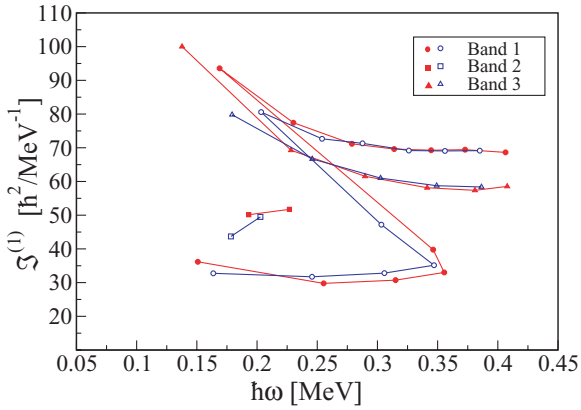

FIG. 9. (Color online) Kinematic moments of inertia ($\mathcal{J}^{(1)}$) as function of rotational frequency ($\hbar\omega$), derived from the experimental γ-ray transitions for the three bands in ^{163}Ta. The positive (negative) signatures are indicated with solid (open) symbols.

the Nilsson states close to the Fermi level. The low excitation energy of the bandhead, the alignment, and the enhanced moment of inertia suggest that this band could be formed by coupling the odd $h_{11/2}$ proton to an octupole vibration. Enhanced octupole collectivity in ^{163}Ta might arise because of the proximity of the proton Fermi level to Nilsson states emanating from the $h_{11/2}$ and $d_{5/2}$ spherical subshells and the neutron Fermi level to the $i_{13/2}$ and $f_{7/2}$ spherical subshells, respectively, differing by $\Delta j = \Delta l = 3$. The coupling of a 3^- octupole phonon to the yrast $[514]9/2^-$ quasiproton configuration would yield spin and parity $I^\pi = 15/2^+$ for the octupole vibrational bandhead, which is consistent with the bandhead spin assignment of Band 2. The relative excitation energy of the $15/2^+$ state is 1313 keV above the bandhead of Band 1 (the $9/2^-$ state) and would thus represent the excitation energy of the octupole phonon. The octupole-vibrational phonon can generate an alignment of $3\hbar$ [37], and the alignment carried by Band 2 is indeed 3–4$\hbar$ higher than for Band 1. The strong $E1$ transitions connecting Band 2 with Band 1 render further support for assigning Band 2 to an octupole vibrational structure.

To gauge the strength of the $E1$ transitions connecting Band 2 with Band 1, $B(E1)/B(E2)$ ratios have been extracted for the $19/2^+, 21/2^+$, and $23/2^+$ states. The $B(E1)$ and $B(E2)$ values are deduced according to the prescription in Ref. [38]. The extracted values are listed in Table III. The observation of enhanced $E1$ strength, with $B(E1) > 10^{-5}$ W.u., is often taken as evidence for octupole correlations in nuclei (see, e.g., Refs. [39–41]). All the values for the γ-ray transitions assigned $E1$ multipolarity are significantly above 10^{-5} W.u., suggesting strong octupole collectivity in ^{163}Ta.

Although plausible, the $\pi h_{11/2}[514]9/2^- \otimes 3^-$ $(e \otimes 3^-)$ configuration assignment to Band 2 remains tentative and further experimental information is needed to elucidate its structure.

C. Band 3

Band 3 carries an alignment of $\sim 10\hbar$ at $\hbar\omega \approx 0.25$ MeV (see Fig. 5), which suggests a 3qp configuration. In the neighboring even-even isotone to ^{163}Ta, ^{162}Hf, the lowest 2qp configuration has been proposed to be formed by coupling an $i_{13/2}$ neutron to an $f_{7/2}$ neutron [E(F) configuration] originating from the $[523]5/2^-$ orbital [25]. The alignment for the AE(F) configuration in ^{162}Hf relative to the ground-state band is $\Delta i_x \sim 9\hbar$ at $\hbar\omega = 0.25$ MeV. This difference in aligned angular momentum compares favorably with the experimental alignment difference of $\Delta i_x \sim 9.2\hbar$ at $\hbar\omega = 0.25$ MeV between Band 1 and Band 3 in ^{163}Ta (see Fig. 5). Hübel *et al.* [25] assigned the AE crossing in ^{162}Hf to occur roughly at the same frequency as the AB crossing ($\hbar\omega \approx 0.28$ MeV).

In Fig. 6(b), the calculated $B(M1; I \to I-1)/B(E2; I \to I-2)$ values are plotted for different configuration assignments together with the experimentally deduced values. The best fit to the data points is obtained with the proposed eAE 3qp configuration. For comparison, the eAB (dotted line) and the cAB (dashed line) configurations are also indicated. Considering the arguments given above, Band 3 is assigned as the positive-parity 3qp eAE ($\pi h_{11/2}[514]9/2^- \otimes \nu i_{13/2}[660]1/2^+ \otimes \nu f_{7/2}[523]5/2^-$) configuration. It is worth noting that such configuration assignments have also been made for similar bands in several neighboring isotopes (e.g., ^{167}Re [7], ^{162}Hf [25], and ^{163}Lu [9]). We also note that Band 3 connects only to Band 2 and not directly to Band 1 via any linking transitions. This is consistent with the $\pi h_{11/2} \otimes \nu i_{13/2} \otimes \nu f_{7/2}$ 3qp configuration, which may exhibit strong octupole mixing, and its wave function may therefore have a large overlap with the proposed $\pi h_{11/2} \otimes 3^-$ configuration of Band 2.

TABLE III. Measured electric dipole ($E1$) strength in Band 2. $B(E2)$ values have been calculated assuming a quadrupole deformation of $Q_0 = 430\ e\,\mathrm{fm}^2$ (taken from TRS calculations).

E_γ (keV)	$B(E1)/B(E2)$ (10^{-8} fm^{-2})	$B(E1)$ ($10^{-5}\ e^2$ fm^2)	$B(E1)$ (10^{-5} W.u.)[a]
855	13.7(10)	94.6(69)	50(5)
900	6.8(7)	30.9(32)	16(2)
649	5.9(5)	40.7(34)	22(3)

[a]1 W.u. = 1.87 e^2 fm^2 for ^{163}Ta.

V. SUMMARY

A level scheme has been established for ^{163}Ta for the first time comprising three band structures. The yrast structure (Band 1) has been interpreted as a 1qp configuration at low spins based on the $[514]9/2^-$ Nilsson orbital. For the states with $I \leqslant 31/2\hbar$, the band shows a large signature splitting, which can be attributed to a triaxial shape with $\gamma < 0°$. At higher spins, the signature splitting disappears as the band forms an axially symmetric 3qp (eAB configuration) structure after the $(\nu i_{13/2})^2$ paired band crossing. Two additional strongly coupled structures have been observed (Bands 2 and 3). Band 2 is tentatively assigned to be built on the odd $h_{11/2}$ proton coupled to an octupole phonon, forming a positive-parity $\pi h_{11/2}[514]9/2^- \otimes 3^-$ configuration. Band 3

is assigned to be associated with the 3qp $\pi h_{11/2} \otimes \nu i_{13/2} \otimes \nu f_{7/2}$ (eAE) configuration based on the deduced alignments and $B(M1)/B(E2)$ ratios.

ACKNOWLEDGMENTS

The authors thank the crew at the Accelerator Laboratory at the University of Jyväskylä for their excellent technical support. Further support for this work has been provided by the Swedish Research Council, the Göran Gustafsson Foundation, the Academy of Finland under the Finnish Centre of Excellence Programme 2006–2011 (Project No. 44875, Nuclear and Condensed Matter Physics Programme at JYFL), the UK Science and Technology Facilities Council and the European Union Fifth Framework Programme "Improving Human Potential—Access to Research Infrastructure" (Contract No. HPRI-CT-1999-00044), the Nordic Infrastructure support by NordForsk (Project 070315), and the Turkish Atomic Energy Authority (TAEK) under Project No. DPT-04K120100-4. C.S. and P.T.G. acknowledge support from the Finnish Academy (Contract No. 209430-111965). We also thank the UK/France (EPSRC/IN2P3) Detector Loan Pool and the EUROBALL owners committee (γ-pool network) for the loan of the EUROGAM detectors of JUROGAM and GSI for the loan of two additional VEGA clover detectors.

[1] D. G. Roux *et al.*, Phys. Rev. C **63**, 024303 (2001).
[2] K. Theine *et al.*, Nucl. Phys. **A536**, 418 (1992).
[3] D. J. Hartley *et al.*, Phys. Rev. C **74**, 054314 (2006).
[4] D. Seweryniak *et al.*, Phys. Rev. C **71**, 054319 (2005).
[5] A. Keenan *et al.*, Phys. Rev. C **63**, 064309 (2001).
[6] M. Sandzelius *et al.*, Phys. Rev. C **75**, 054321 (2007).
[7] D. T. Joss *et al.*, Phys. Rev. C **68**, 014303 (2003).
[8] P. Bringel *et al.*, Phys. Rev. C **73**, 054314 (2006).
[9] D. R. Jensen *et al.*, Nucl. Phys. **A703**, 3 (2002).
[10] S. Frauendorf and F. R. May, Phys. Lett. **B125**, 245 (1983).
[11] C. W. Beausang *et al.*, Nucl. Instrum. Methods Phys. Res. A **313**, 37 (1992).
[12] C. Rossi Alvarez *et al.*, Nucl. Phys. News **3**(3), 10 (1993).
[13] M. Leino *et al.*, Nucl. Instrum. Methods Phys. Res. B **99**, 653 (1995).
[14] M. Leino, Nucl. Instrum. Methods Phys. Res. B **126**, 320 (1997).
[15] R. D. Page *et al.*, Nucl. Instrum. Methods Phys. Res. B **204**, 634 (2003).
[16] I. H. Lazarus *et al.*, IEEE Trans. Nucl. Sci. **48**, 567 (2001).
[17] P. Rahkila, Nucl. Instrum. Methods Phys. Res. A **595**, 637 (2008).
[18] E. S. Paul *et al.*, Phys. Rev. C **51**, 78 (1995).
[19] R. S. Simon, K.-H. Schmidt, F. P. Heßberger, S. Hlavac, M. Honusek, G. Münzenberg, H.-G. Clerc, U. Gollerthan, and W. Schwab, Z. Phys. A **325**, 197 (1986).
[20] E. Hagberg, X. J. Sun, V. T. Koslowsky, H. Schmeing, and H. Hardy, Phys. Rev. C **45**, 1609 (1992).
[21] B. Singh and A. R. Farhan, Nucl. Data Sheets **89**, 1 (2000).
[22] D. C. Radford *et al.*, Nucl. Instrum. Methods Phys. Res. A **361**, 297 (1995).
[23] G. D. Dracoulis, B. Fabricius, P. M. Davidson, A. O. Macchiavelli, J. Oliviera, J. Burde, F. Stephens, and M. A. Deleplanque, in *Proceedings of the International Conference on Nuclear Structure at High Angular Momentum, Ottawa, 1992* (Atomic Energy of Canada, Limited, Ottawa, 1992), AECL-10613, Vol. 2, p. 94.
[24] J. Simpson *et al.*, J. Phys. G: Nucl. Part. Phys. **17**, 511 (1991).
[25] H. Hübel, M. Murzel, E. M. Beck, H. Kluge, A. Kuhnert, K. H. Maier, J. C. Bacelar, M. A. Deleplanque, R. M. Diamond, and F. S. Stephens, Z. Phys. A **329**, 289 (1988).
[26] J. Simpson (private communication).
[27] S. M. Harris, Phys. Rev. **138**, B509 (1965).
[28] X. H. Zhou *et al.*, Eur. Phys. J. A **19**, 11 (2004).
[29] R. A. Bark *et al.*, Nucl. Phys. **A657**, 113 (1999).
[30] D. Dönau and S. Frauendorf, in *Proceedings of the Conference on High Angular Momentum Properties of Nuclei, Oak Ridge*, edited by N. R. Johnson (Harwood, New York, 1983), p. 143.
[31] F. Dönau *et al.*, Nucl. Phys. **A471**, 469 (1987).
[32] K. L. G. Heyde, *The Nuclear Shell Model* (Springer-Verlag, Berlin, Heidelberg, 1994), p. 174.
[33] W. Nazarewicz *et al.*, Nucl. Phys. **A503**, 285 (1989).
[34] W. Satula and R. Wyss, Phys. Scr. **T56**, 159 (1995).
[35] A. J. Kreiner, M. A. J. Mariscotti, C. Baktash, E. derMateosian, and P. Thieberger, Phys. Rev. C **23**, 748 (1981).
[36] National Nuclear Data Center, http://www.nndc.bnl.gov.
[37] J. F. C. Cocks *et al.*, Phys. Rev. Lett. **78**, 2920 (1997).
[38] H. Morinaga and T. Yamazaki, *In-Beam Gamma-ray Spectroscopy* (North-Holland, Amsterdam/New York/Oxford, 1976), p. 68.
[39] J. F. Smith *et al.*, Phys. Lett. **B523**, 13 (2001).
[40] E. S. Paul *et al.*, Phys. Rev. C **50**, R534 (1994).
[41] E. S. Paul *et al.*, Nucl. Phys. **A673**, 31 (2000).